AIAA JOURNAL
Vol. 40, No. 6, June 2002

Advanced Algorithms for Microscale Particle Image Velocimetry

S. T. Wereley* and L. Gui†
Purdue University, West Lafayette, Indiana 47907-1288
and
C. D. Meinhart‡
University of California, Santa Barbara, Santa Barbara, California 93106

The recent explosive increase in the use of fluidic microelectromechanical systems (MEMS) has subsequently driven the development of fluidic measurement techniques capable of measuring velocities at length scales small enough to be of use in characterizing and optimizing these new devices. Recently, several techniques have demonstrated spatial resolutions smaller than 100 μm but larger than 10 μm. These techniques include x-ray microimaging, molecular tagging velocimetry, and microlaser Doppler velocimetry. However, measurements with spatial resolutions smaller than 10 μm are necessary for making measurements in many MEMS applications. Only microparticle image velocimetry has demonstrated this high spatial resolution. By the use of a combination of advanced imaging and processing techniques that are described here, spatial resolutions on the order of single micrometers can be achieved. These techniques are used to investigate the flow though a microfabricated thruster geometry.

I. Introduction

THERE are several areas in science and engineering where it is important to determine the flow field at the micrometer scale. Industrial applications of microfabricated fluidic devices are present in the aerospace, computer, automotive, and biomedical industries. In the aerospace industry, for instance, micrometer-scale supersonic nozzles measuring approximately 35 μm are being designed for the Jet Propulsion Laboratory/NASA to be used as microthrusters on microsatellites and for the Air Force Office of Scientific Research/Defence Advanced Research Agency as flow control devices for palm-size microaircraft.[1] In the computer industry, inkjet printers, which consist of an array of nozzles with exit orifices on the order of tens of micrometers in diameter, account for 65% of the computer printer market.[2] The biomedical industry is currently developing and using microfabricated fluidic devices for patient diagnosis, patient monitoring, and drug delivery. The I-STAT device (Affymetrix, Inc.) is the first microfabricated fluidic device that has been widely used in the medical community for blood analysis. Other examples of microfluidic devices for biomedical research include microscale flow cytometers for cancer cell detection,[3] micromachined electrophoretic channels for DNA fractionation, and polymerase chain reaction chambers for DNA amplification.[4] The details of the fluid motion through these small channels, coupled with nonlinear interactions between macromolecules, cells, and the surface-dominated physics of the channels create very complicated phenomena, which can be difficult to simulate numerically.

There has been a wide range of diagnostic techniques developed for experimental microfluidic research. Some of these techniques have been designed to obtain the highest spatial resolution and velocity resolution possible, whereas other techniques have been designed for application in nonideal situations where optical access is limited,[5] or in the presence of highly scattering media.[6]

Scalar image velocimetry (SIV) was developed by Dahm et al.[7] for measurement of turbulent jets. A variation on SIV, molecular tagging velocimetry (MTV) is a technique that has shown promise in microfluidics research. In this technique, flow-tracing molecules phosphoresce after being excited by a grid of UV light. Two charge-coupled device (CCD) cameras image the phosphorescent grid lines with a short time delay between the two images. Local velocity vectors are estimated by correlating the grid lines between the two images.[8] Paul et al.[9] applied MTV to estimate velocity fields for pressure- and electrokinetically driven flows in 75-μm-diam capillary tubes. Because MTV uses molecular tracers to follow the flow, it has several advantages at the microscale over techniques such as particle image velocimetry (PIV) or laser Doppler velocimetry (LDV), which use discrete flow-tracing particles. However, molecular tracers have much higher diffusion coefficients that may significantly lower the spatial resolution and velocity resolution of the measurements.

The machine vision community developed a class of velocimetry algorithms, called optical-flow algorithms, to determine the motion of rigid objects. The technique can be extended to fluid flows by assuming the effect of molecular diffusion is negligible and requiring that the velocity field is sufficiently smooth. Because the velocity field is computed from temporal and spatial derivatives of the image field, the accuracy and reliability of the velocity measurements is strongly influenced by noise in the image field. This technique imposes a smoothness criterion on the velocity field, which effectively low-pass filters the data and can lower the spatial resolution of the velocity measurements.[10] High-speed x-ray microimaging techniques were presented by Leu et al.[5] A synchrotron is used to generate high-intensity x rays that scatter off the emulsion droplets onto a phosphorous screen. A CCD camera imaging the phosphorous screen detects variations in the scattered x-ray field. The primary advantage of x-ray imaging technique is that one can obtain structural information about the flowfield, without having optical access. Hitt et al.[11] applied the optical-flow algorithm to in vivo blood flow in microvascular networks, with diameters $\sim$100 μm. The algorithm spectrally decomposes subimages into discrete spatial frequencies by correlating the different spatial frequencies to obtain to obtain flowfield information. The advantage of this technique is that it does not require discrete particle images to obtain reliable velocity information. Hitt et al.[12] obtained in vivo images of blood cells flowing through a microvascular network using a 20$\times$ water immersion lens with a spatial resolution on the order of 20 μm in all directions.

LDV has been a standard optical measurement technique in fluid mechanics over the past 25 years. In the case of a dual-beam LDV system, the volume of the intersection of the two laser beams defines the measurement volume. Traditionally, the measurement volumes of standard LDV systems have characteristic dimensions on the order of a few millimeters. Compton and Eaton[13] used

Presented as Paper 2001-0243 at the AIAA 39th Aerospace Sciences Meeting, Reno, NV, 8–11 January 2001; received 12 March 2001; revision received 20 November 2001; accepted for publication 21 November 2001. Copyright © 2002 by the American Institute of Aeronautics and Astronautics, Inc. All rights reserved. Copies of this paper may be made for personal or internal use, on condition that the copier pay the $10.00 per-copy fee to the Copyright Clearance Center, Inc., 222 Rosewood Drive, Danvers, MA 01923; include the code 0001-1452/02 $10.00 in correspondence with the CCC.

*Assistant Professor, Mechanical Engineering Department.
†Postdoctoral Researcher, Mechanical Engineering Department.
‡Associate Professor, Department of Mechanical and Environmental Engineering.

short-focal-length optics to obtain a measurement volume of 35×66 μm. Using very short-focal-lengthlenses, Tieu et al.[14] built a dual-beamsolid-stateLDA system that has a measurement volume of approximately 5×10 μm. Their micro-LDV system was used to measure the flow through a 175-μm-thick channel, producing time-averaged measurements that compare well to the expected parabolic velocity profile, except within 18 μm of the wall. Advancements in microfabrication technology are expected to facilitate the development of new generations of self-contained solid-state LDV systems with micrometer-scale probe volumes. These systems will likely serve an important role in diagnosis and monitoring of microfluidic systems. However, the size of the probe volume significantly limits the number of fringes that it can contain, which subsequently limits the accuracy of the velocity measurements.

Optical Doppler tomography (ODT) has been developed to measure micrometer-scale flows embedded in a highly scattering medium. In the medical community, the ability to measure in vivo blood flow under the skin allows clinicians to determine the location and depth of burns.[6] ODT combines single-beam Doppler velocimetry, with heterodyne mixing from a low-coherence Michelson interferometer. The lateral spatial resolution of the probe volume is determined by the diffraction spot size. The Michelson interferometer is used to limit the effective longitudinal length of the measurement volume to that of the coherence length of the laser. The ODT system developed by Chen et al.[6] has a lateral and longitudinal spatial resolution of 5 μm and 15 μm, respectively. The system was applied to measure flow through a 580-μm-diam conduit.

PIV can be used to obtain high spatial resolution two-dimensional velocity fields. Santiago et al.[15] demonstrated a micro-PIV system capable of measuring slow flows, velocities on the order of hundreds of micrometers per second, with a spatial resolution of $6.9 \times 6.9 \times 1.5$ μm. The system used an epifluorescent microscope and an intensified CCD camera to record 300-nm-diam polystyrene flow-tracing particles. The particles are illuminated using a continuous Hg-arc lamp. The continuous Hg-arc lamp is chosen for situations that require low levels of illumination light, for example, flows containing living biological specimens, and where the velocity is sufficiently small so that the particle motion can be frozen by the CCD camera's electronic shutter.

Later applications of the micro-PIV technique moved steadily toward faster flows more typical of aerospace applications. The Hg-arc lamp was replaced with a New Wave Research two-headed Nd:YAG laser that allowed cross correlation analysis of singly exposed image pairs acquired with submicrosecond time steps between images. At macroscopic length scales, this short time step would allow analysis of supersonic flows. However, because of the high magnification, the maximum velocity measurable with this time step is on the order of meters per second. Meinhart et al.[16] applied micro-PIV to measure the flowfield in a 30 μm high $\times$ 300 μm wide rectangular channel, with a flow rate of 50 μl/h, equivalent to a centerline velocity of 10 mm/s or three orders of magnitude faster than the initial effort a year before. The experimental apparatus, shown in Fig. 1, images the flow with a 60$\times$, numerical aperture (NA) = 1.4, oil-immersion lens. The 200-nm-diam polystyrene flow-tracing particles were chosen small enough so that they faithfully followed the flow and were 150 times smaller than the smallest channel dimension. A subsequent investigation by Meinhart and Zhang[17] of the flow inside a microfabricated ink jet printer head yielded the highest speed measurements made with micro-PIV. Using a slightly lower magnification (40$\times$) and consequently lower spatial resolution, measurements of velocities as high as 8 m/s were made. In the following sections the authors will give an overview of micro-PIV techniques and provide several application examples.

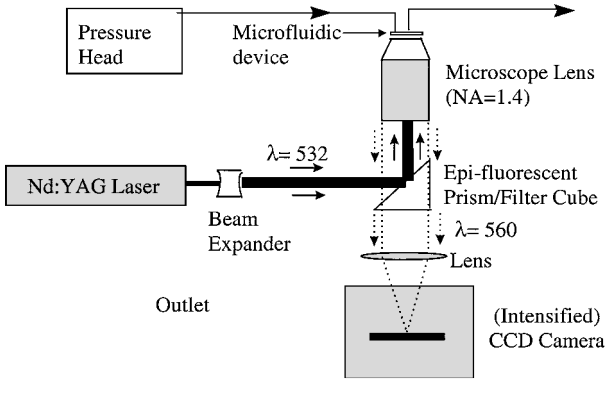

Fig. 1 Diagram of typical micro-PIV system.

II. Overview of Micro-PIV

A. Fundamental Physics Considerations of Micro-PIV

Three fundamental problems differentiate micro-PIV from conventional macroscopic PIV: The particles become small compared to the wavelength of the illuminating light, the particles become small enough that the effects of Brownian motion must be addressed, and the illumination source is typically not a light sheet but rather an illuminated volume of the flow.

1. *Particles Small Compared to* λ

Flow-tracing particles must also be large enough to scatter sufficient light so that their images can be recorded. In the Rayleigh scattering regime, where the particle diameter d is much smaller than the wavelength of light, $d \ll \lambda$, the amount of light scattered by a particle varies as d^{-6} (Ref. 18). Because the diameter of the flow-tracing particles must be small enough that the particles not disturb the flow being measured, they can frequently be on the order of 50–100 nm. Their diameters are then $\frac{1}{10}$–$\frac{1}{5}$ the wavelength of green light, $\lambda = 532$ nm, and are, therefore, approaching the Rayleigh scattering criteria. This places significant constraints on the image recording optics, making it extremely difficult to record particle images.

One solution to the imaging problem is to use epifluorescence imaging to record light emitted from fluorescently labeled particles, using an optical filter to remove the background light. This technique was used successfully in liquid flows to record images of 200–300 nm diam fluorescent particles.[15,16] Although fluorescently labeled particles are well suited for micro-PIV studies in liquid flows, they are not applicable to high-speed airflows for several reasons. Commercially available fluorescently labeled particles are available only in aqueous solutions. In principle, the particle-laden solutions can be dried, and the particles emitted into an airstream. Unfortunately, we have not been able to dry particles without significant particle clumping. Furthermore, the emission decay time of many fluorescent molecules is on the order of several nanoseconds, which may cause streaking of the particle images for high-speed flows. Presently, seeding gas flows remains a significant problem in micro-PIV.

2. *Effects of Brownian Motion*

When the seed particle size becomes small, the collective effect of collisions between the particles and a moderate number of fluid molecules is unbalanced, preventing the particle from following the flow to some degree. Santiago et al.[15] considered the effect of Brownian motion on the accuracy of PIV measurements. When it is assumed that seed particles having an Einstein diffusion coefficient D are in a steady, uniform flow of velocity u for a time duration Δt, one can estimate the relative error due to Brownian motion ε_B by

$$\varepsilon = 1/u\sqrt{2D/\Delta t} \tag{1}$$

Santiago et al.[15] considered a flow with a characteristic velocity of $u \sim 50$ μm s^{-1}; diffusion coefficient of the 300 nm particles is $D \sim 0.69$ μm^2 s^{-1}, and time between images is $\Delta t = 68.5$ ms, yielding a relative error of approximately 9% for a single particle. Because this error results from random Brownian motion of water molecules bombarding the flow-tracing particles, it is an unbiased error that can be reduced by averaging over groups of particles. Because each PIV interrogation region contains a small group of particles and the resulting cross correlation function is ensemble averaged over several realizations, the error in the resulting velocity vector is substantially reduced. When it is assumed that each particle in the ensemble of interrogation regions contributes equally to the average velocity vector and that they are statistically independent,

the uncertainty due to Brownian motion of the ensemble-averaged velocity is approximately $\varepsilon_B/\sqrt{N}$, where N is the total number of particles in the average.

Equation (1) demonstrates that the effect of Brownian motion is relatively less important for faster flows. However, for a given measurement, when u increases, Δt will generally be decreased. Equation (1) also demonstrates that when all conditions but the Δt are fixed, going to larger Δt will decrease the relative error introduced by Brownian motion. Unfortunately, longer Δt will decrease the accuracy of the results because the PIV measurements are based on a first-order accurate approximation to the velocity. Using a second-order accurate technique [called central difference interrogation (CDI) and presented later] allows for longer Δt to be used without increasing this error.

3. Volume Illumination of Flow

The third significant difference between micro-PIV and macroscopic PIV is that, due to lack of optical access along with significant diffraction in light sheet forming optics, light sheets are typically not a practical source of illumination for microflows. Consequently, the flow must be volume illuminated, leaving two choices for how to visualize the seed particles: with an optical system whose depth of focus exceeds the depth of the flow being measured or with an optical system whose depth of focus is small compared to that of the flow. Both of these techniques have been used in various implementations of micro-PIV. Cummings[19] uses a large depth of focus imaging system to explore electrokinetic and pressure-driven flows. The advantage of the large depth of focus optical system is that all particles in the field of view of the optical system are well focused. The disadvantage of this scheme is that all depth information is lost, and the resulting velocity fields are completely depth averaged. Cummings[19] addresses this problem with advanced processing techniques that will not be covered here.

The second choice of imaging systems is one whose depth of focus is smaller than that of the flow domain. The optical system will then focus those particles that are within the depth of focus of the imaging system while the remaining particles will be unfocused and contribute to the background noise level. Because the optical system is being used to define thickness of the measurement domain, it is important to characterize exactly how thick the depth of focus, or more appropriately, the depth of correlation, is. Meinhart et al.[20] have considered this question in detail and derived the equation

$$\delta z_m = \frac{3n\lambda_0}{\mathrm{NA}^2} + \frac{2.16 d_p}{\tan\theta} + d_p \tag{2}$$

where δz_m is the measurement plane thickness, λ_0 is the collected light wavelength, n is the refractive index of medium the lens is immersed in, NA is the numerical aperture of the optical system, θ is the collection angle of the optical system, and d_p is the diameter of the seed particles. This equation demonstrates that the depth of correlation is a complicated function of experimental parameters that must be carefully evaluated for every experimental situation, even if only a minor variable such as the wavelength of illumination is changed. The depth of correlation can range from 1.8 μm for a 60× oil immersion lens imaging 200-nm particles to 3.4 μm for a 60× oil immersion lens imaging 1-μm particles to 8.6 μm for a 40× air immersion lens imaging 1-mm particles. Olsen and Adrian[21,22] have developed similar expressions from a different approach for both cases in which Brownian motion of the particles is a factor as well as those in which it is not.

One important implication of volume illumination that affects both large and small depth of focus imaging systems is that all particles in the illuminated volume will contribute to the recorded image. This implies that the particle concentrations will have to be minimized for deep flows and leads to the use of low image density images as described next.

B. Special Processing Methods for Micro-PIV Recordings

When evaluating digital PIV recordings with conventional correlation-based algorithms or image-pattern tracking algorithms, a sufficient number of particle images are required in the interrogation window or the tracked image pattern to ensure reliable and accurate measurement results. However, in many cases, especially in micro-PIV measurements, the particle image density in the PIV recordings is usually not high enough, for example, Fig. 2a. These PIV recordings are called low image density (LID) recordings and are usually evaluated with particle-tracking algorithms. When using particle-tracking algorithms, the velocity vector is determined with only one particle, and hence, the reliability and accuracy are of the technique are limited. In addition, interpolation procedures are usually necessary to obtain velocity vectors on the desired regular grid points from the random distributed particle-tracking results (for example, Fig. 3a) and therefore, additional uncertainties are added to the final results. Fortunately, some special processing methods can be used to evaluate the micro-PIV recordings, so that the errors resulting from the LID can be avoided. In this section two methods are introduced to improve measurement accuracy of micro-PIV by using a digital image processing technique and by improving the evaluation algorithm, respectively.

1. Overlapping of LID-PIV Recordings

In early days of PIV, multiple exposure imaging techniques were used to increase the particle image numbers in PIV recordings. Similar to multiply exposing a single frame, high image density (HID) PIV recordings can be generated by computationally overlapping a number of LID-PIV recordings with

$$g_0(x, y) = \max\{g_k(x, y), k = 1, 2, 3, \ldots, N\} \tag{3}$$

where $g_k(x, y)$ is the gray value distributions of the LID-PIV recordings with a total number N and $g_0(x, y)$ is the overlapped recording.

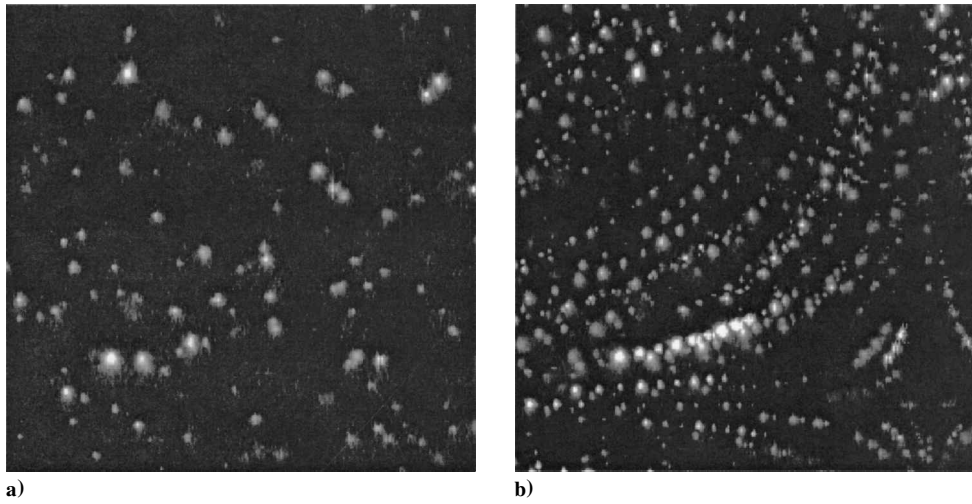

a) b)

Fig. 2 Example of image (size 256 × 256 pixels) overlapping: a) one of the LID-PIV recordings and b) result of overlapping nine LID-PIV recordings.

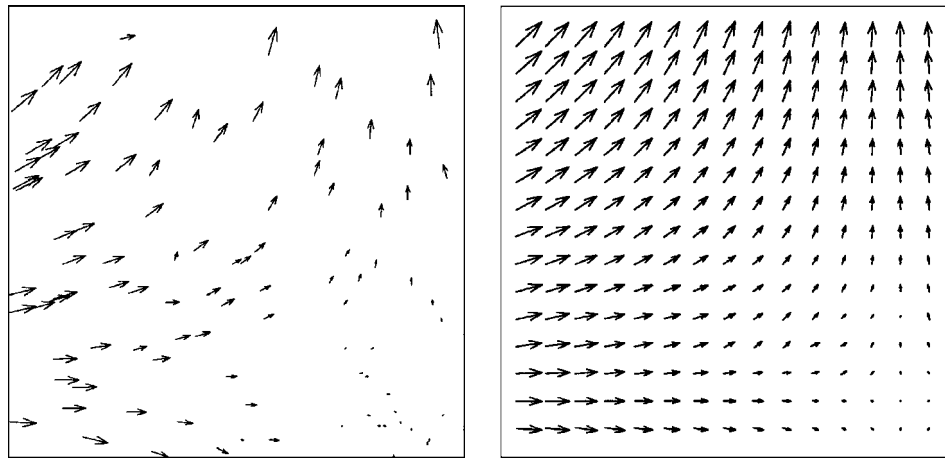

Fig. 3 Effect of image overlapping: a) results for a single LID-PIV recording pair with a particle-tracking algorithm and b) results for the overlapped PIV recording pair with a correlation-based algorithm.

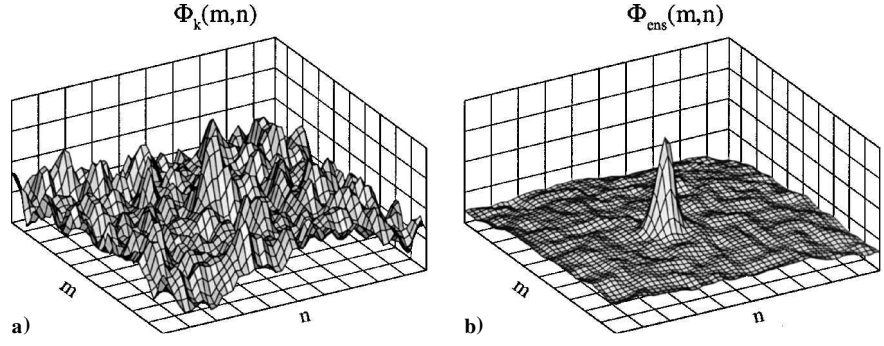

Fig. 4 Effect of ensemble correlation: a) results with conventional correlation for one of the PIV recording pairs and b) results with ensemble correlation for 101 PIV recording pairs.

Note that in Eq. (3) the particle images are positive, that is, with bright particles and dark background; otherwise the images should be inverted or the minimum function used. An example of the image overlapping can be seen in Fig. 2b for overlapping nine LID-PIV recordings. The size of the PIV recordings in Fig. 2 is 256×256 pixels, and the corresponding measurement area is 2.5×2.5 mm^2. The effect of the image overlapping is shown in Fig. 3. Figure 3a is the evaluation results for one of the LID-PIV recording pairs with a particle-tracking algorithm,[23] and Fig. 3b is the results for the overlapped PIV recording pair (out of nine LID-PIV recording pairs) with a correlation-based algorithm. The results in Fig. 3b are more reliable, more dense, and more regularly spaced than those in Fig. 3a.

The image overlapping method is based on that flows in microdomains typically have very low Reynolds numbers, so that the flow can be considered as laminar and steady in the data acquisition period. Note that this method cannot be extended to measurements of turbulent or unsteady flows, and it may not work very well when overlapping HID-PIV recordings or too many LID-PIV recordings because, with large numbers of particle images, interference between particle images will occur.[24] Further study of this technique will be necessary to quantify these limitations, but the promise of the technique is obvious.

2. Ensemble Correlation Method

For correlation-based PIV evaluation algorithms, the correlation function at a certain interrogation spot is usually represented as

$$\Phi_k(m, n) = \sum_{j=1}^{q} \sum_{i=1}^{p} f_k(i, j) \cdot g_k(i + m, j + n) \qquad (4)$$

where $f_k(i, j)$ and $g_k(i, j)$ are the gray value distributions of the first and second exposure, respectively, in the kth PIV recording pair at a certain interrogation spot of size of $p \times q$ pixels. The correlation function for a singly exposed PIV image pair has a peak at the position of the particle image displacement in the interrogation spot (or window), which should be the highest among all of the peaks of Φ_k. The subpeaks, which result from noise or mismatch of particle images, are usually obviously lower than the main peak, that is, the peak of the particle image displacement. However, when the interrogation window does not contain enough particle images or the noise level is too high, the main peak will become weak and may be lower than some of the subpeaks, and as such, an erroneous velocity vector is generated. In the laminar and steady flows measured by the micro-PIV system, the velocity field is independent of the measurement time. That means the main peak of $\Phi_k(m, n)$ is always at the same position for PIV recording pairs taken at different times, whereas the sub peaks appear with random intensities and positions in different recording pairs. Therefore, when averaging Φ_k over a large number of PIV recording pairs, N, the main peak will remain at the same position in each correlation function, but the noise peaks, which occur randomly, will average to zero. The averaged (or ensemble) correlation function is given as

$$\Phi_{\text{ens}}(m, n) = \frac{1}{N} \sum_{k=1}^{N} \Phi_k(m, n) \qquad (5)$$

Just as with the image overlapping method detailed earlier, the ensemble correlation requires a steady flow. However, in contrast with the image overlapping method, the technique is not limited to LID recordings or to a small number of recordings. The concept of averaging correlation functions can also be applied to other evaluation algorithms such as correlation tracking and the minimum quadratic difference (MQD) method. This method was first proposed and demonstrated by Meinhart et al.[24]

The ensemble correlation function technique is demonstrated for 101 LID-PIV recording pairs, Φ_{ens}, in Fig. 4 in comparison to the correlation function for one of the single recording pair, Φ_k. These

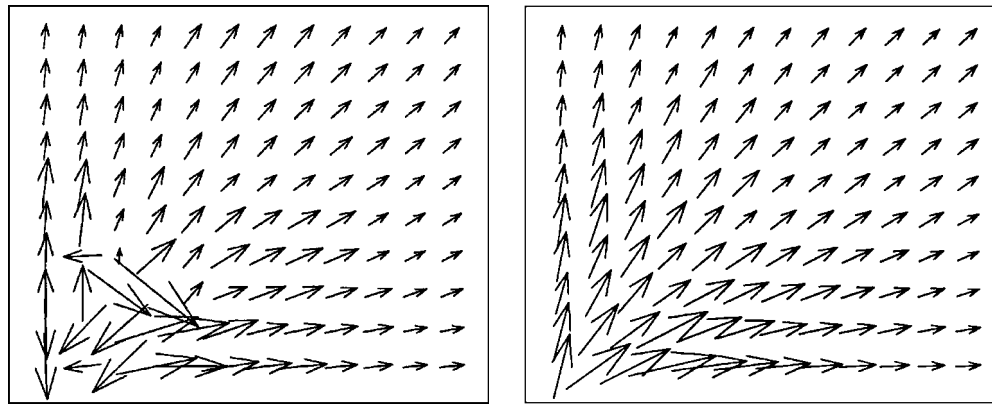

a) b)

Fig. 5 Comparison of the velocity field calculated using a) a single PIV recording pair and b) the average correlation of 101 image pairs.

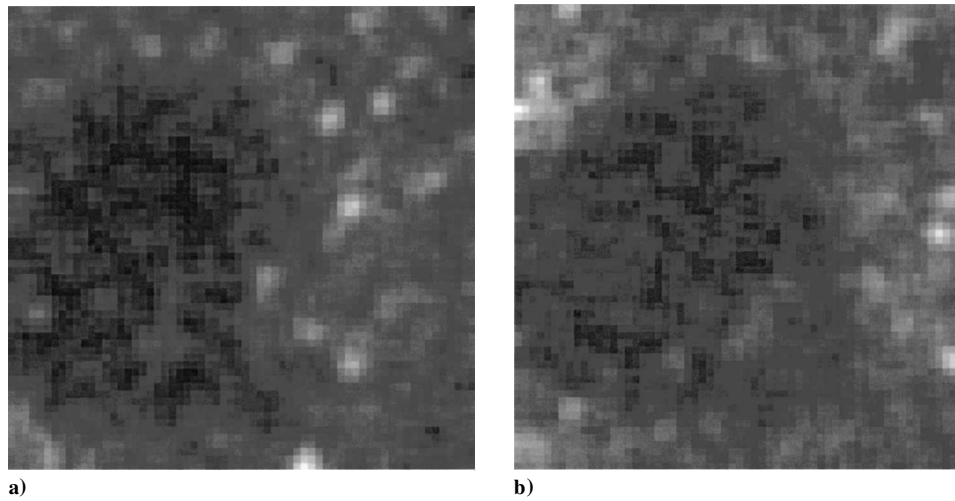

a) b)

Fig. 6 One of PIV image sample pairs from a microchannel measurement (64 × 64 pixels).

PIV recording pairs are chosen from the flow measurement in a microfluidic biochip for impedance spectroscopy of biological species.[25] With the conventional evaluation function in Fig. 4a, the main peak cannot easily be identified among the subpeaks, so that the evaluation result is neither reliable nor accurate. However, the ensemble correlation function in Fig. 4b shows a very clear peak at the particle image displacement, and the subpeaks can hardly be recognized.

The effect of the ensemble correlation technique on the resulting velocity field is demonstrated in Fig. 5 with the PIV measurement of flow in the microfluidic biochip. All of the obvious evaluation errors resulting from the LID and strong background noise (Fig. 5a) are avoided by using the ensemble correlation method based on 101 PIV recording pairs (Fig. 5b). Note that because the unreliable vectors in Fig. 5a all occur at the lower-left-hand corner of the flow domain, removal of these unreliable vectors and subsequent replacement by interpolated vectors will only coincidentally generate results that bear any resemblance to the true velocity field in the device. In addition, if the problem leading to low signal levels in the lower-left-hand corner of the images is systematic, that is, larger background noise, etc., even a large collection of images will not generate better results because they will all have unreliable vectors at the same location.

3. Removing Background Noise

To use the recording overlapping or ensemble correlation techniques, a great number of micro-PIV recording pairs are usually obtained, enabling removal of the background noise from the micro-PIV recording pairs. One of the possibilities for obtaining an image of the background from a large number of PIV recordings is averaging these recordings.[23] Because the particles are randomly distributed and quickly move through the camera view area, their images will disappear in the averaged recording. However, the image of the background (including boundary, contaminants on the glass cover, particles adhered to the wall, etc.) maintains the same brightness distribution in the averaged recording because it does not move or change. Another method is building at each pixel location a minimum of the ensemble of PIV recordings because the minimal gray value at certain pixel may reflect the background brightness in the successively recorded images.[26] The background noise may be successfully removed by subtracting the background image from the PIV recordings.

As an example, Fig. 6 shows a pair of sample images from a PIV measurement in a microchannel. The size of the sample pair is 64 × 64 pixels, and the total sample number is 100 pairs. The mean particle image displacement is about 12.5 pixels from left to right. The particle images in a region at left-hand side of the sample pair look darker than those out of this region. That may result from an asperity on the glass cover of the microchannel. The ensemble correlation function for the 100 image sample pairs without background removal is given in Fig. 7a, which shows a dominant peak near zero displacement because the fleck does not move. When the background image is built with the minimum gray value method and subtracted from the image sample pairs, the influence of the asperity is reduced so that the peak of the particle image displacement appears clearly in the evaluation function in Fig. 7b.

C. Advanced Processing Methods Suitable for Both Micro/Macro-PIV Recordings

To further improve the reliability and accuracy of micro-PIV measurements, a number of evaluation techniques, which also work well for standard PIV systems, are applied. It is known that the measurement uncertainty of PIV data includes both bias error and precision error. One of the most effective methods for reducing the bias error

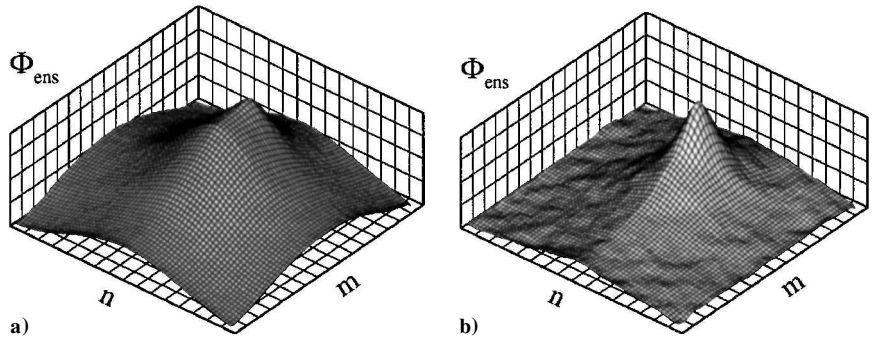

Fig. 7 Ensemble correlation function for 100 image sample pairs a) without and b) with background removal.

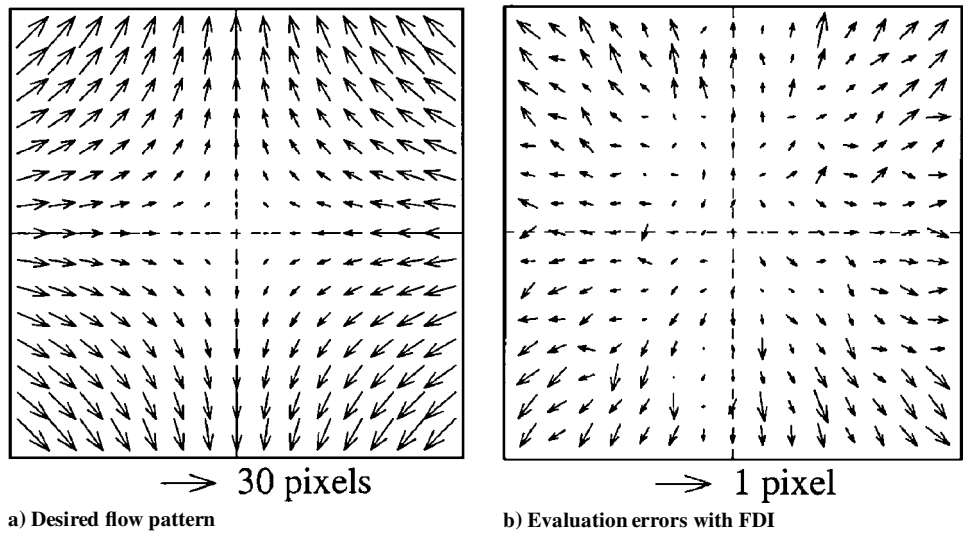

a) Desired flow pattern **b) Evaluation errors with FDI**

Fig. 8 Simulation of the four-roll-mill test.

of PIV measurements in complex flows is the CDI method. For reducing the precision (or random) error, image correction methods are suggested. The CDI method and one of the image correction methods are introduced next.

1. CDI

Currently, adaptive window offsetting is widely used with the fast-Fourier-transform- (FFT-) based correlation algorithm for reducing the evaluation error and with the image pattern tracking algorithms for increasing the spatial resolution. The adaptive window offset method, as typically implemented, can be referred to as forward difference interrogation (FDI) because the second interrogation window is shifted in the forward direction of the flow, an amount equal to the mean displacement of the particle images initially in the first window. Although the FDI method leads to significant improvements in the evaluation quality of PIV recordings in many cases, there are still some potentially detrimental bias errors that cannot be avoided when using an FDI method. The CDI method was developed by Wereley and Meinhart[27] to avoid the shortcoming of FDI and to increase the accuracy of the PIV measurement. The comparison between the CDI and FDI methods is analogous to the comparison between central difference and forward difference discretizations of derivatives wherein the central difference method is accurate to order Δt^2, whereas the forward difference method is only accurate to order Δt. When using CDI, the first and second interrogation windows are shifted backward and forward, respectively, each by half of the expected particle image displacement (see Fig. 3 in Ref. 27). As with many adaptive window shifting techniques, this technique requires iteration to achieve optimum results.

To demonstrate the advantage of CDI over the FDI, a typical curvature flow, that is, the flow in a four-roll mill, is used here as an example. Based on actual experimental parameters, such as particle image size, concentration, and intensity, PIV recording pairs are simulated with the desired flowfield shown in Fig. 8a. The maximal particle image displacement in the PIV recording pair of size of 1024×1024 pixels is about 30 pixels. The corresponding measurement area and the maximal velocity are $10 \times 10\,\text{mm}^2$ and 0.04 mm/s, respectively. When the FFT-based correlation algorithm is combined with FDI, evaluation errors of a pair of the simulated recordings are determined by subtracting the desired flowfield from the evaluation results and are given in Fig. 8b. The evaluation errors in Fig. 8b are obviously dominated by bias errors that depend on the radial position, that is, the distance between the vector location and the flowfield center.

In this test, the bias errors are determined by averaging 500 individual error maps as shown in Fig. 8b, and a distribution of rms values of the random errors is further computed. Dependences of the bias and random errors on the radial position are determined and are shown in Figs. 9a and 9b for the FDI and CDI, respectively. The total error is defined as the rss of the bias and random error. It is shown in Fig. 9 that the evaluation error of FDI is dominated by the bias error, at radial positions greater than 200 pixels. When CDI is used, the bias error is so small that it can be neglected in comparison to the random error that does not depend on the location.

2. Image Correction Technique

In the preceding example, the bias error of the four-roll-mill test is minimized by using the CDI method. To further reduce the measurement uncertainty, that is, the total error, the random errors must also be reduced. In the four-roll-mill test case, even when the flow is ideally seeded and the PIV recordings are made without any noise, evaluation errors may result from the deformation of the measured flow. To account for the deformation of the PIV image pattern, image correction techniques have been developed. The idea of image correction was presented by Huang et al.,[28] and similar ideas were also applied by others. However, because the image correction was

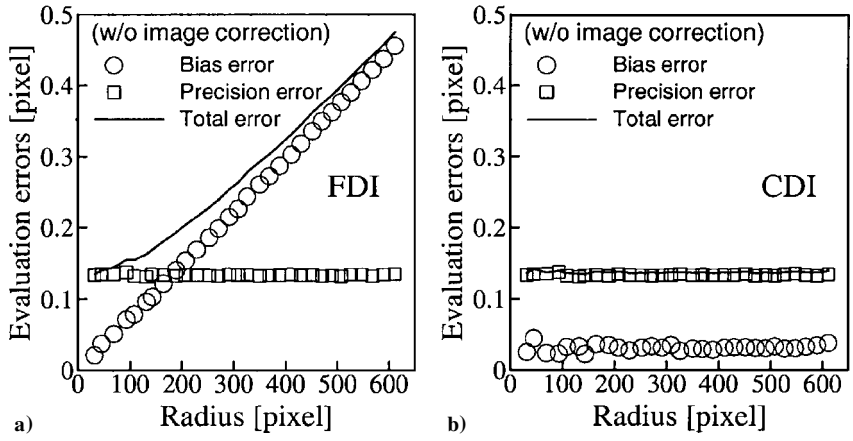

Fig. 9 Four-roll-mill test dependences of evaluation errors on the location (radius) of the evaluation with a) FDI and b) CDI.

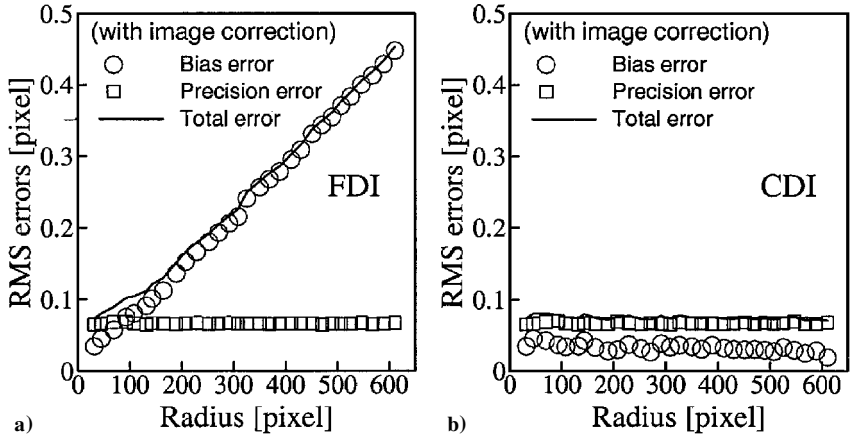

Fig. 10 By use of image correction, dependences of evaluation errors on the location of the evaluation with a) FDI and b) CDI.

a complex and time-consuming procedure, it has not been widely used. To accelerate the evaluation, the authors modified the image correction method as follows: Based on previous iterations, the particle image displacements at the four corners of each interrogation window are calculated and used to deform the image patterns in the interrogation area for both exposures of the PIV recording pair using a simple bilinear interpolation, so that the image patterns have a good match despite spatial velocity gradients at the particle image displacement (see Fig. 1 in Ref. 29). When the modified image correction technique is combined with the FFT-based correlation algorithm, the evaluation can be run at a very high speed. The effect of the image correction is presented in Fig. 10. When Fig. 9 is compared with Fig. 10, the effect of the image correction can be seen to reduce the total error of the measurement scheme by about half.

III. Micro-PIV Examples: Flow in a Micronozzle

The utility of these new imaging and processing algorithms along with the micro-PIV technique itself can be demonstrated by measuring the flow through a micronozzle. The micronozzles were designed to be operated with supersonic gas flows. In the initial stages of this investigation, however, they were operated with a liquid to assess the spatial resolution capabilities of the micro-PIV technique without having to push the temporal envelope simultaneously. The significant issues associated with extending the results presented here to gas-phase flows are further explored by Meinhart et al.[30] Consequently, the converging–diverging geometry of the micronozzle served as a very small venturi. The micronozzles were fabricated by R. Bayt and K. Breuer (now at Brown University) at the Massachusetts Institute of Technology in 1998. The two-dimensional nozzle contours, similar to those shown in Fig. 11, were etched using deep reactive ion etching (DRIE) in 300-μm-thick silicon wafers. The nozzles used in the current experiments were only etched 50 μm deep into a 300-μm-thick silicon wafer. A single 500-μm-thick glass wafer was anodically bonded to the top of the wafer to provide an end wall. The wafers were mounted to a macroscopic aluminum manifold, pressure sealed using number 0 O-rings and vacuum grease and connected with plastic tubing to a Harvard Apparatus syringe pump.

The liquid (deionized water) flow was seeded with relatively large 700-nm-diam fluorescently labeled polystyrene particles (available from Duke Scientific). The particles were imaged using an air-immersion NA = 0.6, 40× objective lens and the epifluorescent imaging system described in Sec. II. A flow rate of 4 ml h^{-1} was delivered to the nozzle by the syringe pump.

Figure 12 is the velocity field inside a nozzle with a 15-deg half-angle and a 28-μm throat. The velocity field was calculated using the CDI technique with image overlapping (10 image pairs) and image correction, as explained earlier. The interrogation windows measured 64 × 32 pixels in the x and y directions, respectively. When projecting into the fluid, the correlation windows were 10.9 × 5.4 μm in the x and y directions, respectively. The interrogation spots were overlapped by 50% in accordance with the Nyquist criterion, yielding a velocity-vector spacing of 5.4 μm in the streamwise direction and 2.7 μm in the spanwise direction. The Reynolds number, based on bulk velocity and throat width, is $Re = 22$.

Turning now from a converging geometry to a diverging geometry, we can explore whether instabilities well predicted by the Reynolds number at macroscopic length scales are indeed as well predicted by the Reynolds number at small length scales. The diffuser has a throat width of 28 μm and a thickness of 50 μm. The divergence half-angle is quite large, 40 deg. The expected behavior for this geometry would be that at low Reynolds number the flow would be entirely Stokes flow, that is, no separation, but at larger Reynolds numbers where inertial effects become important, separation should appear. Indeed this is just what happens. At a Reynolds number of 22, the flow in the diverging section of the nozzle remains

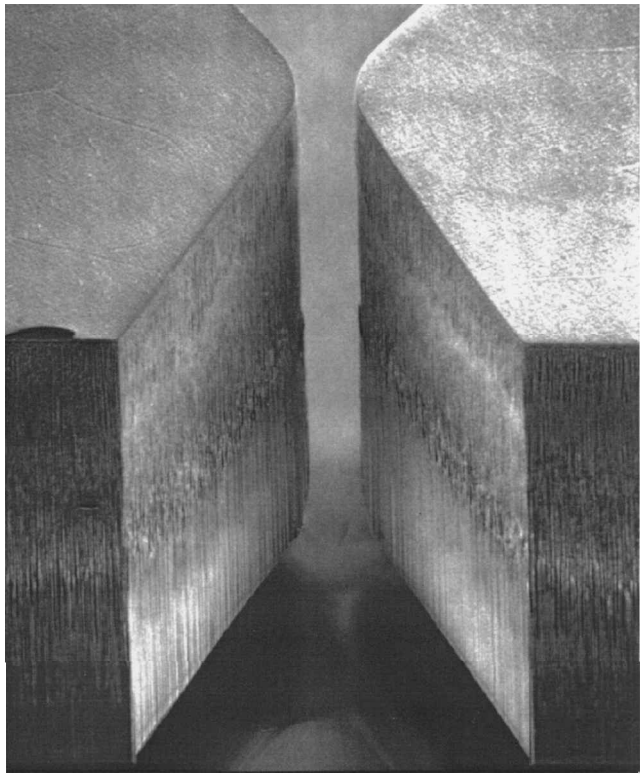

Fig. 11 Scanning electron micrograph of DRIE microthruster geometry; throat width is 19 μm and the thickness is 300 μm. (Courtesy of K. Breuer at Brown University.)

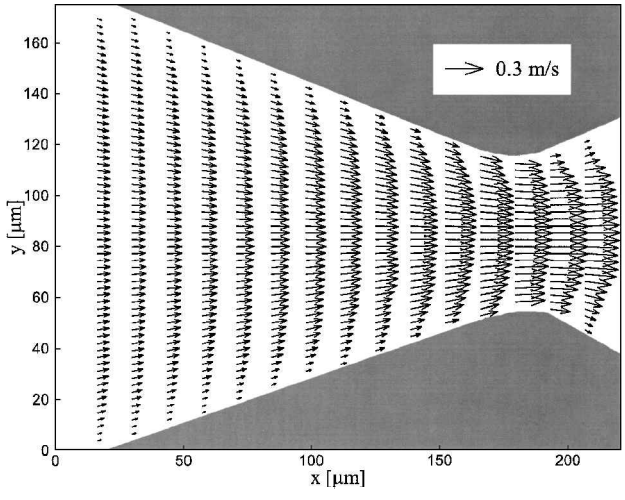

Fig. 12 Velocity field produced from 10 overlapped image pairs; spatial resolution is 10.9 μm in the horizontal direction and 5.4 μm in the vertical. For clarity only every fifth column of measurements is shown.

attached to the wall (not shown), whereas at a Reynolds number of 83, the flow separates as shown in Figs. 13a and 13b. Figures 13 are based on a single pair of images and as such represent an instantaneous snapshot of the flow. Figure 13b is a closeup view of the vortical region of the flow produced from the same velocity data used to produce Fig. 13a. The interrogation region size measured 32×32 pixels^2 or 5.4×5.4 μm^2. A close inspection of Fig. 13 reveals that the separation creates a stable, steady vortex standing at the point of separation. After the flow has dissipated some of its energy in the vortex, it no longer has sufficient momentum to exist as a jet, and it reattaches to the wall immediately downstream of the vortex. This is arguably the smallest vortex ever measured. Considering that the Kolmogorov length scale is frequently on the order of 0.1–1.0 mm, micro-PIV has more than enough spatial resolution to measure turbulent flows at, and even significantly below, the Kol-

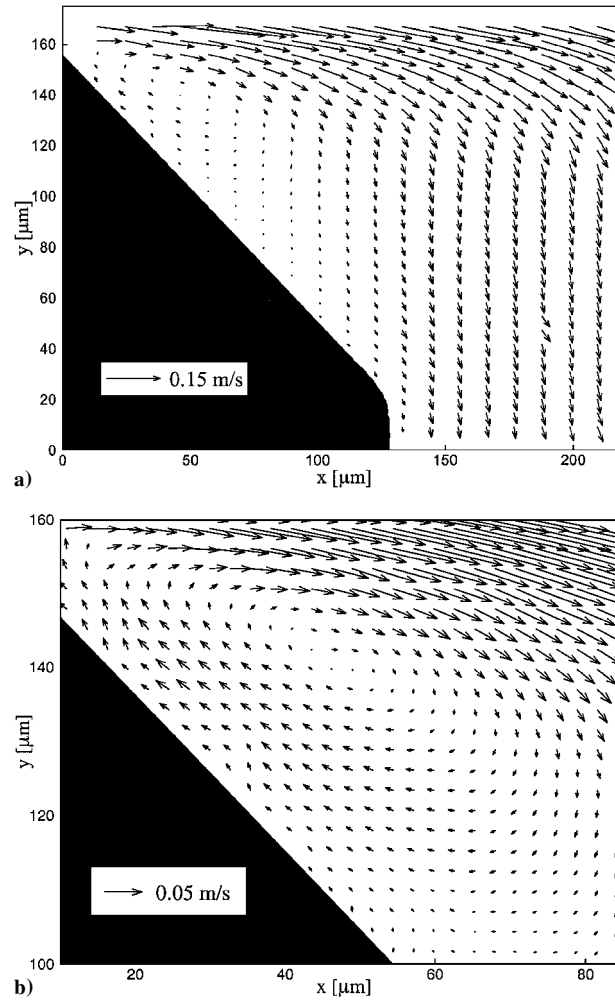

Fig. 13 Recirculation regions in a microdiffuser with spatial resolution of 5.4 × 5.4 mm^2: a) zoomed out view with only every fourth column and every second row shown and b) closeup view of vortex region with all rows and columns of data shown.

mogorov length scale. The example shown has 25 vectors measured across the 60-μm extent of the vortex.

IV. Conclusions

Currently, when all of the advanced techniques outlined here are applied, the maximum spatial resolution of the micro-PIV technique stands at approximately 1 μm. By the use of smaller seed particles that fluoresce at shorter wavelengths, this limit could be reduced by a factor of 2–4. This lower limit of approximately 250 nm should be regarded as a hard limit for correlation-based PIV using visual wavelength light. Higher spatial resolutions could still be obtained by adding a particle-tracking step after the correlation-based PIV. Spatial resolutions an order of magnitude smaller could then reasonably be reached.

The algorithm advances presented have been demonstrated to allow measurements at length scales on the order of 1 μm, significantly below the typical Kolmogorov length scale. These spatial resolutions are indispensable when analyzing flows in microdomains or the smallest scales of turbulence. The most significant problem standing in the way of extending micro-PIV to gas-phase flows is seeding. With adequate seeding, the results presented here can be extended to gas flows.

Acknowledgments

This work was supported by the Indiana 21st Century Research and Technology Fund, the School of Mechanical Engineering at Purdue University, and the 3M Corporation. The simulated four-roll-mill data were inspired by Gary Leal and Derek Tretheway at the University of California, Santa Barbara.

References

[1]Bayt, R. L., and Breuer, K. S., "Fabrication and Testing of Micron-Sized Cold-Gas Thrusters in Micropropulsion of Small Spacecraft," Vol. 187, Progress in Astronautics and Aeronautics, edited by M. Micci and A. Ketsdever, AIAA, Reston, VA, 2000, pp. 381–398.

[2]Kamisuki, S., Hagata, T., Tezuka, C., Nose, Y., Fujii, M., and Atobe, M., "A Low Power, Small, Electrostatically-Driven Commercial Inkjet Head," *Proceedings of MEMS'98*, Inst. of Electrical and Electronics Engineers, New York, 1998, pp. 63–68.

[3]Fuller, C. K., Hamilton, J., Ackler, H., Krulevitch, P., Boser, B., Eldredge, A., Becker, F., Yang, J., and Gascoyne, P., "Microfabricated Multi-Frequency Particle Impedance Characterization System," *Proceedings Micro Total Analysis Systems*, Kluwer Academic Publishers, Dordrecht, The Netherlands, 2000.

[4]Northrup, M. A., Hills, R. F., Landre, R., Lehew, H. D., and Watson, R. A., "A MEMS-Based DNA Analysis System," *Eighth International Conference on Solid State Sensors and Actuators*, Foundation for Sensor and Actuator Technology, Stockholm, 1995, pp. 764–767.

[5]Leu, T. S., Lanzillotto, A. M., Amabile, M., and Wildes, R., "Analysis of Fluidic and Mechanical Motions in MEMS by Using High Speed X-Ray Micro-Imaging Techniques," *1997 International Conference on Solid-State Sensors and Actuators, Transducers 97*, Vol. 1, Inst. of Electrical and Electronics Engineers, New York, 1997, pp. 149, 150.

[6]Chen, Z., Milner, T. E., Dave, D., and Nelson, J. S., "Optical Doppler Tomographic Imaging of Fluid Flow Velocity in Highly Scattering Media," *Optics Letters*, Vol. 22, No. 1, 1997, pp. 64–66.

[7]Dahm, W. J. A., Su, L. K., and Southerland, K. B., "A Scalar Imaging Velocimetry Technique for Fully Resolved Four-Dimensional Vector Velocity Field Measurements in Turbulent Flows," *Physics of Fluids A (Fluid Dynamics)*, Vol. 4, No. 10, 1992, pp. 2191–2206.

[8]Koochesfahani, M. M., Cohn, R. K., Gendrich, C. P., and Nocera, D. G., "Molecular Tagging Diagnostics for the Study of Kinematics and Mixing in Liquid Phase Flows," *Proceedings in the Eighth International Symposium on Applications of Laser Techniques to Fluid Mechanics*, Calouste Gulbenkian Foundation, Lisbon, 1996.

[9]Paul, P. H., Garguilo, M. G., and Rakestraw, D. J., "Imaging of Pressure- and Electrokinetically-Driven Flows Through Open Capillaries," *Analytical Chemistry*, Vol. 70, pp. 2459–2467.

[10]Wildes, R. P., Amable, M. J., Lanzilloto, A. M., and Leu, T. S., "Physically Based Fluid Flow Recovery from Image Sequences," *Proceedings of the IEEE Conference on Computer Vision and Pattern Recognition, 1997*, Inst. of Electrical and Electronics Engineers, New York, 1997, pp. 969–975.

[11]Hitt, D. L., Lowe, M. L., Tincher, J. R., and Watters, J. M., "A New Method for Blood Velocimetry in the Microcirculation," *Microcirculation*, Vol. 3, No. 3, 1996, pp. 259–263.

[12]Hitt, D. L., Lowe, M. L., and Newcomer, R., "Application of Optical Flow Techniques to Flow Velocimetry," *Physics of Fluids*, Vol. 7, No. 1, 1995, pp. 6–8.

[13]Compton, D. A., and Eaton, J. K., "A High-Resolution Laser Doppler Anemometer for Three-Dimensional Turbulent Boundary Layers," *Experiments in Fluids*, Vol. 22, No. 2, 1996, pp. 111–117.

[14]Tieu, A. K., Mackenzie, M. R., and Li, E. B., "Measurements in Microscopic Flow with a Solid-State LDA," *Experiments in Fluids*, Vol. 19, No. 4, 1995, pp. 293, 294.

[15]Santiago, J. G., Wereley, S. T., Meinhart, C. D., Beebe, D. J., and Adrian, R. J., "A Particle Image Velocimetry System for Microfluidics," *Experiments in Fluids*, Vol. 25, No. 4, 1998, pp. 316–319.

[16]Meinhart, C. D., Wereley, S. T., and Santiago, J. G., "PIV Measurements of a Microchannel Flow," *Experiments in Fluids*, Vol. 27, No. 5, 1999, pp. 414–419.

[17]Meinhart, C. D., and Zhang, H., "The Flow Structure Inside a Microfabricated Inkjet Printer Head," *Journal of Microelectromechanical Systems*, Vol. 9, No. 1, 2000, pp. 67–75.

[18]Born, M., and Wolf, E., *Principles of Optics*, *Pergamon*, Oxford, 1997, p. 661.

[19]Cummings, E. B., "An Image Processing and Optimal Nonlinear Filtering Technique for PIV of Microflows," *Experiments in Fluids*, Vol. 29, No. 7, 2000, pp. S42–S50.

[20]Meinhart, C. D., Wereley, S. T., and Gray, M. H. B., "Depth Effects in Volume Illuminated Particle Image Velocimetry," *Measurement Science and Technology*, Vol. 11, 2000, pp. 809–814.

[21]Olsen, M. G., and Adrian, R. J., "Out-of-Focus Effects on Particle Image Visibility and Correlation in Particle Image Velocimetry," *Experiments in Fluids*, No. 7, 2000, pp. S166–S174.

[22]Olsen, M. G., and Adrian, R. J., "Brownian Motion and Correlation in Particle Image Velocimetry," *Optics and Laser Technology*, Vol. 32, 2000, pp. 621–627.

[23]Gui, L., Merzkirch, W., and Shu, J. Z., "Evaluation of Low Image Density PIV Recordings with the MQD Method and Application to the Flow in a Liquid Bridge," *Journal of Flow Visualization and Image Processing*, Vol. 4, No. 4, 1997, pp. 333–343.

[24]Meinhart, C. D., Wereley, S. T., and Santiago, J. G., "A PIV Algorithm for Estimating Time-Averaged Velocity Fields," *Journal of Fluids Engineering*, Vol. 122, 2000, pp. 285–289.

[25]Gomez, R., Bashir, R., Sarakaya, A., Ladisch, M. R., Sturgis, J., Robinson, J. P., Geng, T., Bhunia, A. K., Apple, H. L., and Wereley, S. T., "Microfluidic Biochip for Impedance Spectroscopy of Biological Species," *Biomedical Microdevices*, Vol. 3, No. 3, 2001, pp. 201–209.

[26]Cowen, E. A., and Monismith, S. G., "A Hybrid Digital Particle Tracking Velocimetry Technique," *Experiments in Fluids*, Vol. 22, No. 3, 1997, pp. 199–211.

[27]Wereley, S. T., and Meinhart, C. D., "Adaptive Second-Order Accurate Particle Image Velocimetry," *Experiments in Fluids*, Vol. 31, No. 3, 2001, pp. 258–268.

[28]Huang, H., Dabiri, D., and Gharib, M., "On Error of Digital Particle Image Velocimetry," *Measurement Science and Technology*, Vol. 8, No. 12, 1997, pp. 1427–1440.

[29]Wereley, S. T., and Gui, L. C., "PIV Measurement in a Four-Roll-Mill Flow with a Central Difference Image Correction (CDIC) Method," 4th International Symposium on Particle Image Velocimetry, German Aerospace Center (DLR) Göttingen, Germany, Paper 1027, Sept. 2001.

[30]Meinhart, C. D., Gray, M. H. B., and Wereley, S. T., "PIV Measurements of High-Speed Flows in Silicon-Micromachined Nozzles," AIAA Paper 99-3756, 1999.

W. R. Lempert
Guest Associate Editor